Supplementary Information

Nanoarchitectonics of cobalt/nitrogen-doped carbon with unbalanced double primitive bicontinuous motif for efficient electrocatalysis

Bin Zhao,[a] Bohan Liu,[a] Ji Han,[a] Ruigang Sun,[a] Haidong Xu,[a] Yuanbo Sun,[ab] Guangrui Chen,[ac] Zhaohui Shi,[a] Chenxu Liu,[a] Yanjing Gao,[a] Mingjie Zhang,[a] Song Lin Zhang,[d] Yusuke Yamauchi,[efg] and Buyuan Guan*[ac]

a. State Key Laboratory of Inorganic Synthesis and Preparative Chemistry, College of Chemistry, Jilin University, Qianjin Street 2699, Changchun 130012, P. R. China

b. Key Lab of Groundwater Resources and Environment, Ministry of Education, Jilin University, Changchun 130021, P. R. China

c. International Center of Future Science, Jilin University, Qianjin Street 2699, Changchun 130012, P. R. China

d. Institute of Materials Research and Engineering (IMRE), Agency for Science, Technology and Research (A*STAR), 2 Fusionopolis Way, Singapore 138634, Singapore

e. School of Chemical Engineering and Australian Institute for Bioengineering and Nanotechnology (AIBN), The University of Queensland, Brisbane QLD 4072, Australia

f. Department of Materials Process Engineering, Graduate School of Engineering, Nagoya University, Furo-cho, Chikusa-ku, Nagoya, Aichi, 464-8603, Japan

g. Department of Chemical and Biomolecular Engineering, Yonsei University, 50 Yonseiro, Seodaemun-gu, Seoul 03722, Republic of Korea

[*] E-mail: guanbuyuan@jlu.edu.cn

Supporting Information

Table of Contents

Section 1. Supplementary methods

Chemicals

Commercial reagents were purchased and used as received unless otherwise noted. Dichloromethane (Macklin, 99.0%), methoxypolyethylene glycols (Macklin, average M_n ~2000), 2-bromoisobutyryl bromide (Innochem, 98.0%), triethylamine (Innochem, 99.5%), diethyl ether (Sinopharm Chemical Reagent Company), 4-dimethylaminopyridine (Innochem, 99.0%), cuprous bromide (CuBr, Innochem, 99.0%), 1,1,4,7,7-pentamethyl-diethylenetriamin (PMDETA, Innochem, 98.0%), styrene (St, Macklin), ascorbic acid (Innochem, 99.0%), 1,4-dioxane (Diox, Macklin, 99.0%), *N,N*-dimethylformamide (DMF, Macklin, 99.5%), cobalt (II) acetate tetrahydrate ($Co(Ac)_2 \cdot 4H_2O$, Aladdin), cobaltous nitrate hexahydrate ($Co(NO_3)_2 \cdot 6H_2O$, Macklin), zinc bromide ($ZnBr_2$, Macklin), 2-methylimidazole (2-MIM, Aladdin, 98.0%), methanol (Sinopharm Chemical Reagent Company, 99.5%), ethanol (Sinopharm Chemical Reagent Company, 99.5%), tetrahydrofuran (THF, Macklin, 99.0%), potassium hydroxide (KOH, Aladdin), chloroform-*d* ($CDCl_3$, Macklin, 99.8% + 0.03% TMS), aluminum oxide (Al_2O_3, Sinopharm Chemical Reagent Company), Nafion solution (Innochem, 5 wt %), Pt/C (Innochem, 20%), and deionized (DI) water from Milli-Q integral water purification system (Millipore, 18.2 $M\Omega \cdot cm^{-1}$).

Synthesis of bicontinuous polymer cubosomes

PS_{218}-*b*-PEO_{45} was prepared by atom transfer radical polymerization according to the literature.[1] 30 mg of PS-*b*-PEO was dissolved in a mixture of 2.75 mL of Diox and 0.24 mL of DMF, and then 3.8 mL of water was slowly dropped into the solution under gentle stirring. The resulting self-assembly was poured into 25 mL of water for centrifugation and purification. The residual organic solvent was washed away with water, and the sample was dried overnight in vacuum at room temperature.

Synthesis of ZIF-8 SPPs

10 mg of PCs and 40 mg of 2-MIM were dispersed in a mixture of 10 mL of water and 5 mL of methanol. The mixture was sonicated for 30 s and stirred for 2 h. Then, 12.5 mg of $ZnBr_2$ was added into the above mixture and stirred for 1 h at room temperature. The product was centrifuged and

washed three times with DMF to remove the template, and dried overnight in vacuum at room temperature.

Synthesis of ZIF-8@ZIF-67 SPPs and Co/NC UDPPs

20 mg of ZIF-8 SPPs was dispersed in 4.8 mL of methanol solution containing 24 mg of $Co(NO_3)_2 \cdot 6H_2O$. The mixture was then added into 1.6 mL of methanol solution containing 52 mg of 2-MIM at room temperature and gently stirred for 24 h. The product was centrifuged and washed with ethanol three times and dried overnight in vacuum at room temperature. Finally, the ZIF-8@ZIF-67 SPPs were heated to 700 °C at a rate of 1 °C min^{-1} under nitrogen atmosphere and kept at 700 °C for 3 h to obtain Co/NC UDPPs.

Synthesis of ZIF-67 crystals and Co/NC SPs

Typically, 0.6 g of $Co(Ac)_2 \cdot 4H_2O$ and 2.24 g of 2-MIM were dissolved in 5.0 mL of H_2O respectively to form two clear solutions. Subsequently, the solution of 2-MIM was poured into the solution of $Co(Ac)_2 \cdot 4H_2O$. Then, the mixture was stirred for 15 s and allowed it to stand at room temperature for 5 h. The product was centrifuged and washed with ethanol five times and dried overnight in vacuum at room temperature. Finally, the ZIF-67 crystals were heated to 700 °C at a rate of 1 °C min^{-1} under nitrogen atmosphere and kept at 700 °C for 3 h to obtain Co/NC SPs.

Synthesis of ZIF-67 SPPs and Co/NC SPPs

10 mg of PCs and 70 mg of 2-MIM were dispersed in a mixture of 2.25 mL of water and 0.75 mL of methanol. The mixture was sonicated for 30 s and stirred for 2 h. Then, 10.8 mg of $Co(NO_3)_2 \cdot 6H_2O$ was added into the above mixture and stirred for 15 min at room temperature. The product was centrifuged and washed three times with DMF to remove the template, and dried overnight in vacuum at room temperature. Finally, the ZIF-67 SPPs were heated to 700 °C at a rate of 1 °C min^{-1} under nitrogen atmosphere and kept at 700 °C for 3 h to obtain Co/NC SPPs.

Characterizations

Nuclear Magnetic Resonance (NMR) spectroscopy was recorded at room temperature using a Bruker Avance Neo spectrometer operating at frequencies of 400 MHz for ^1H. Gel Permeation

Chromatography (GPC) analysis was performed on a Waters 2414 Refractive Index Detector. Scanning Electron Microscopy (SEM) images were measured with Hitachi SU8020 electron microscope. Transmission Electron Microscopy (TEM) images and the elemental mapping were acquired with Tecnai F20 and JEM-F200 electron microscope. Small-Angle X-ray Scattering (SAXS) measurements were completed on a Xeuss 3.0 equipped with a Cu Kα microfocus source. Powder X-ray Diffraction (XRD) measurements were performed on a Malvernpanalytical Empyrean diffractometer by using Cu Kα radiation. Nitrogen adsorption/desorption measurements were carried out on Micromeritics ASAP 2420 analyzer at 77 K after the samples were degassed at 120 °C for 10 h under vacuum. Thermogravimetric Analysis (TGA) measurements were performed on STA 449 F5 Jupiter at a heating rate of 5 °C min^{-1} from room temperature to 800 °C in nitrogen. Raman spectra was carried out on LabRAM HR Evolution. X-ray Photoelectronic Spectroscopy (XPS) measurements were performed on Thermo ESCALAB 250 with Al Kα radiation as the X-ray source.

Electrochemical measurements

The ORR catalytic performances were conducted on an electrochemical workstation (CHI760E) with a three-electrode system at the ambient temperature in 0.1 M KOH alkaline electrolyte solution, using the glassy carbon rotating disk electrode (RDE)/ rotating ring disk electrode (RRDE) as a working electrode, carbon rod as a counter electrode, and saturated calomel electrode (SCE) as a reference electrode. All potential values were calibrated to the reversible hydrogen potential (E_{RHE}) based on the Nernst equation of $E_{\mathrm{RHE}} = E_{\mathrm{SCE}} + 0.0592 \times \mathrm{pH} + 0.241$. The ink of each catalyst was prepared by dispersing 2 mg of catalyst in 0.5 mL of mixed solvent containing 5 μL Nafion solution and 495 μL water. The homogeneous ink was obtained by ultrasonication for an hour. 25 μL of ink was dropped on the RDE glass carbon electrode with a diameter of 5 mm, and 30 μL of ink was dropped on the RRDE glass carbon electrode with a diameter of 5.61 mm. The RDE tests were conducted using linear sweep voltammetry (LSV) at a scan rate of 10 mV s^{-1} in the potential window of 0.1-1.2 V (vs. RHE) in O_2 saturated 0.1 M KOH electrolyte with varying speeds of 900-2500 rpm. The RRDE experiments were also tested in O_2 saturated 0.1 M KOH. The i-t chronoamperometric responses were carried at 0.7 V and performed in O_2 saturated 0.1 M KOH at 1600 rpm for 30000 s. Based on the results of the RRDE test, the electron transfer number (n) and hydrogen peroxide yield (H_2O_2%) were calculated:

$$\mathrm{n} = \frac{4I_D}{I_D + I_R/N}$$

$$\mathrm{H_2O_2\%} = \frac{I_R/N}{I_D + I_R/N} \times 200\%$$

where I_D is the disk current; I_R is the ring current, and N is the collection efficiency of the ring current ($N = 0.37$).

The K-L equations can be used to analyze kinetic parameters as following:

$$\frac{1}{J} = \frac{1}{J_K} + \frac{1}{J_L} = \frac{1}{J_K} + \frac{1}{B\omega^{1/2}}$$

$$B = 0.2nFC_0(D_0)^{2/3}\upsilon^{-1/6}$$

Where J represents the measured current density, J_K is the kinetic current density, J_L is the limiting diffusion current density, ω is the electrode rotating rate, F is the Faraday constant (96485 C mol^{-1}), C_0 is the bulk concentration of O_2 0.1 M KOH (1.26×10^{-6} mol cm^{-3}), D_0 is the oxygen diffusion coefficient (1.9×10^{-5} cm^2 s^{-1}) of 0.1 M KOH, and ν is the kinematic viscosity of 0.1 M KOH (0.01 cm^2 s^{-1}).

The zinc-air battery tests were performed in home-made electrochemical cells. A polished Zn plate with a thickness of 0.20 mm was used as the anode. Then, 6 M KOH aqueous solution with 0.2 M $Zn(Ac)_2$ was used as the electrolyte. Typically, the air cathode was fabricated by spraying the catalyst ink onto the hydrophobic carbon paper, and the Ni foam as a current collector. The catalyst ink was prepared by mixing 5 mg of electrocatalysts with 50 μL of 5 %Nafion (Dupont) solution and 450 μL of ethanol solution. The mass loading of the catalysts was calculated to be 1 mg cm^{-2}. The corresponding electrochemical test was carried out with an electrochemical workstation (CHI 660E) and LAND CT2001A multi-channel battery testing system (Wuhan, China). The galvanostatic discharge–charge cycle performance of the zinc-air batteries was evaluated with the cycling tests (10 min discharge followed by 10 min charge, at a current density of 10 mA cm^{-2}). The specific capacity assessment of the zinc-air battery was tested at a current density of 5 mA cm^{-2}, and the corresponding calculation method was as follows:

Specific capacity (mAh g^{-1}) = "Discharge current (mA) × Service time (h)" / "The weight of consumed zinc (g)"

Finite Element Simulation

The simulation process of electrocatalyst model is performed by finite element method based on COMSOL Multiphysics 6.2 platform. Based on the TEM images of samples, the 3*3*3 structural unit (side length: 200 nm) of the materials with different pore structure is used as the model to simulate the localized reaction environment. The left and right sides of the model are designated as electrolyte inlet and outlet respectively, and the O_2 concentration in the solution is set to 1.2 mol m^{-3} and the OH^- concentration is set to 0.1 mol L^{-1}. In addition, a constant oxygen reduction reaction rate is set on the model. The following are the main equations used in the simulation.

Navier-Stokes equation:

$$\rho\left(\frac{\partial u}{\partial t} + u\,\nabla u\right) = -\nabla p + \nabla\left(\mu\left(\nabla u + (\nabla u)^T\right) - \frac{2}{3}\mu(\nabla\, u)I\right) + F$$

where u is fluid velocity, p is fluid pressure, ρ is fluid density, μ is dynamic viscosity, and F is the external force acting on the fluid.

Darcy's law:

$$\frac{\partial \varepsilon_p \rho}{\partial t} + \nabla\,\rho u = 0$$

$$u = -\frac{\kappa}{\mu}(\nabla p + \rho g \nabla D)$$

where ρ is fluid density, t is time, ε_p is porosity factor, u is Darcys velocity, $\kappa$is permeability, μ is the dynamic viscosity, p is fluid pressure, g is gravitational acceleration, and D is elevation.

Fick's laws of diffusion:

$$N_i = -D_i \nabla c_i$$

where N_i is molar flux, D_i is diffusion coefficient, and c_i is concentration.

Section 2. Supplementary Figures

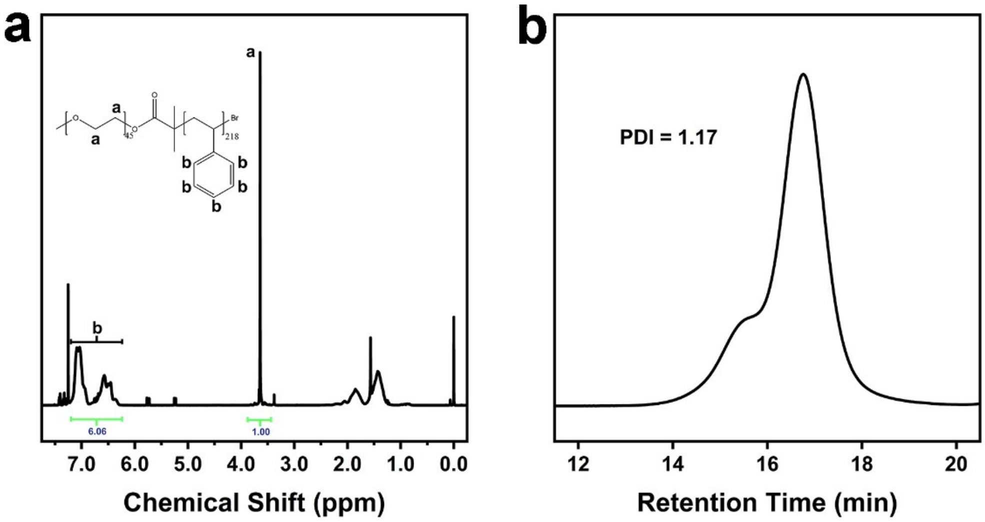

Fig. S1 (a) ^{1}H NMR spectrum in $CDCl_3$ and (b) GPC result of the PS_{218}-*b*-PEO_{45} copolymer.

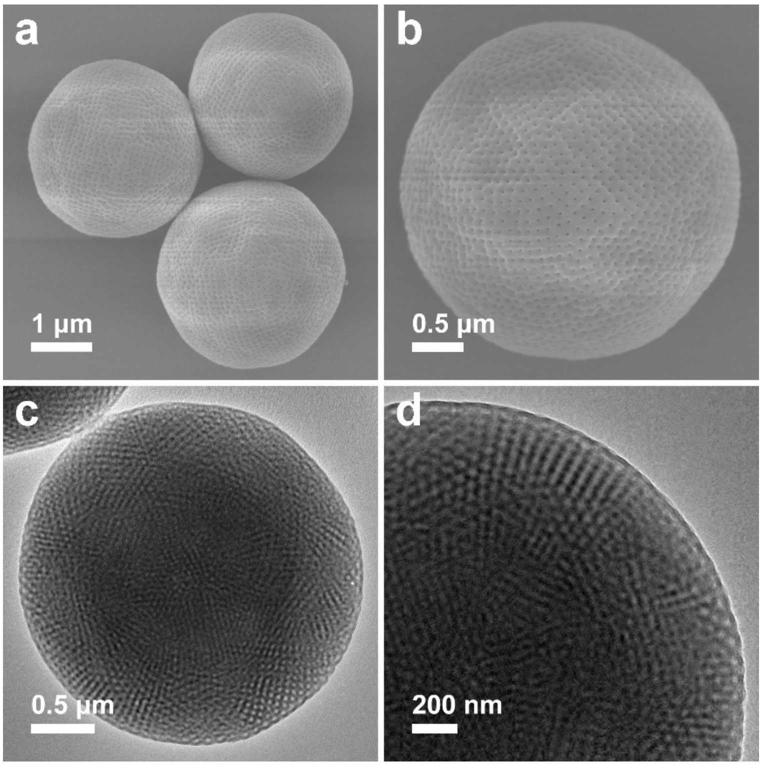

Fig. S2 (a,b) SEM and (c,d) TEM images of PCs.

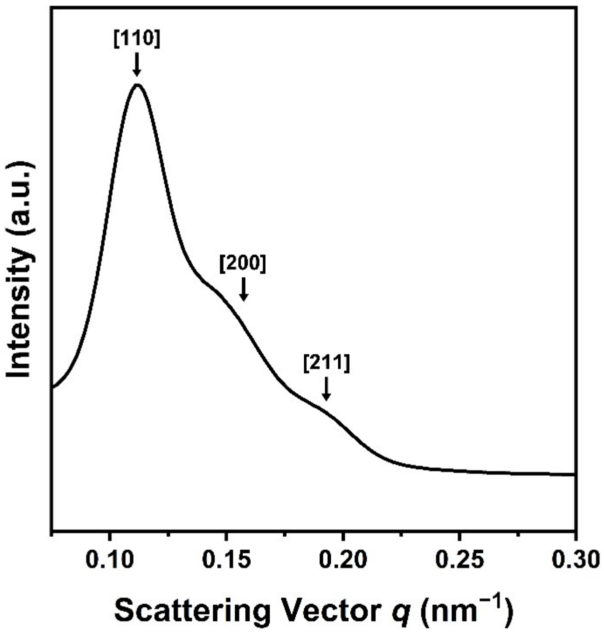

Fig. S3 SAXS pattern of PCs.

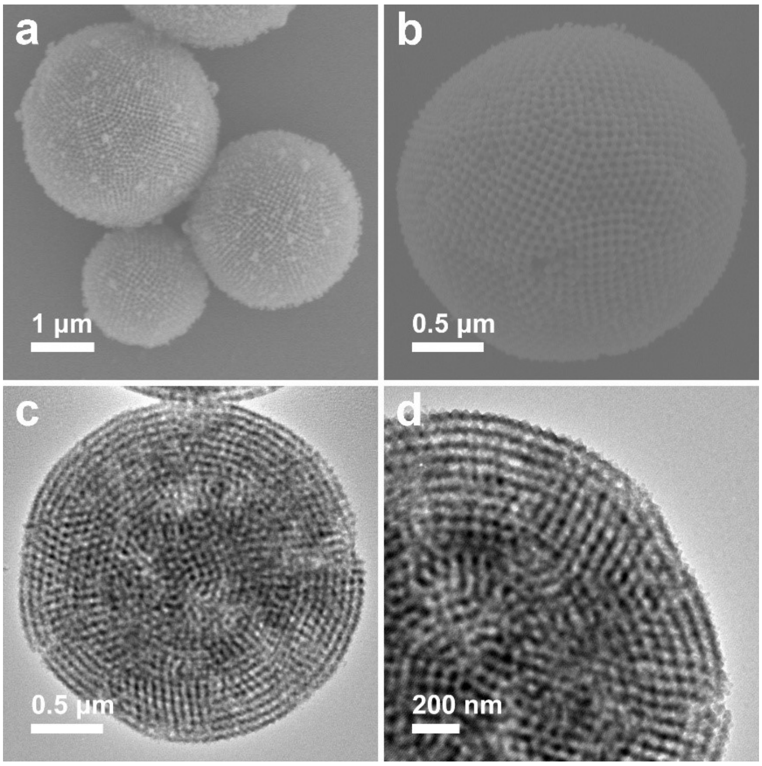

Fig. S4 (a,b) SEM and (c,d) TEM images of ZIF-8 SPPs.

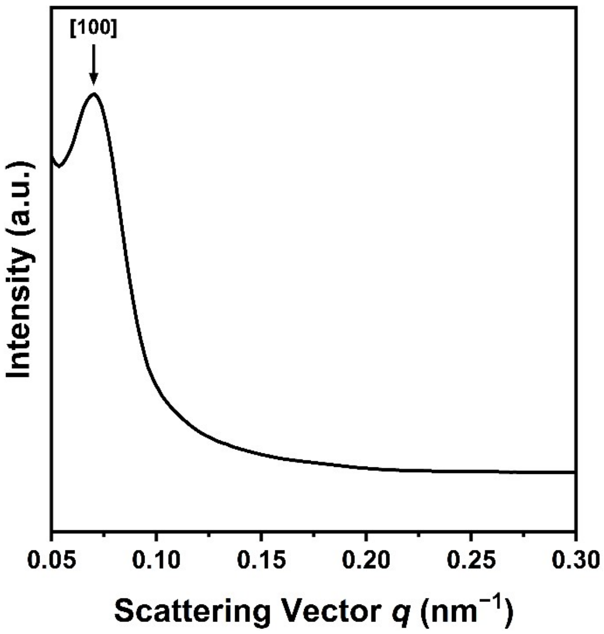

Fig. S5 SAXS pattern of ZIF-8 SPPs.

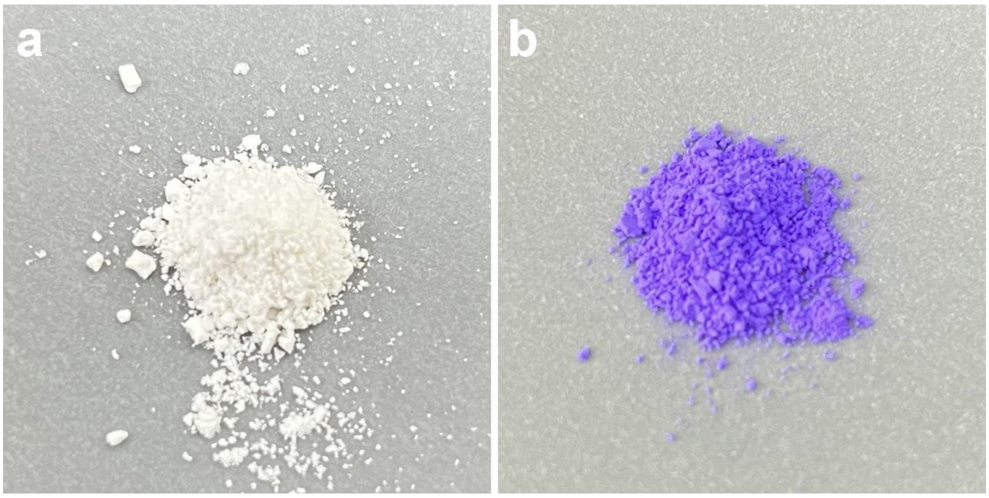

Fig. S6 Photographs of the powders of (a) ZIF-8 SPPs and (b) ZIF-8@ZIF-67 SPPs.

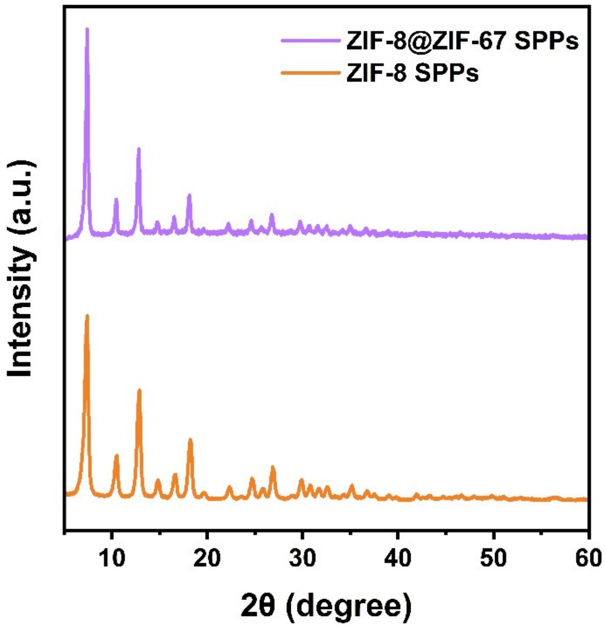

Fig. S7 XRD patterns of ZIF-8 SPPs and ZIF-8@ZIF-67 SPPs.

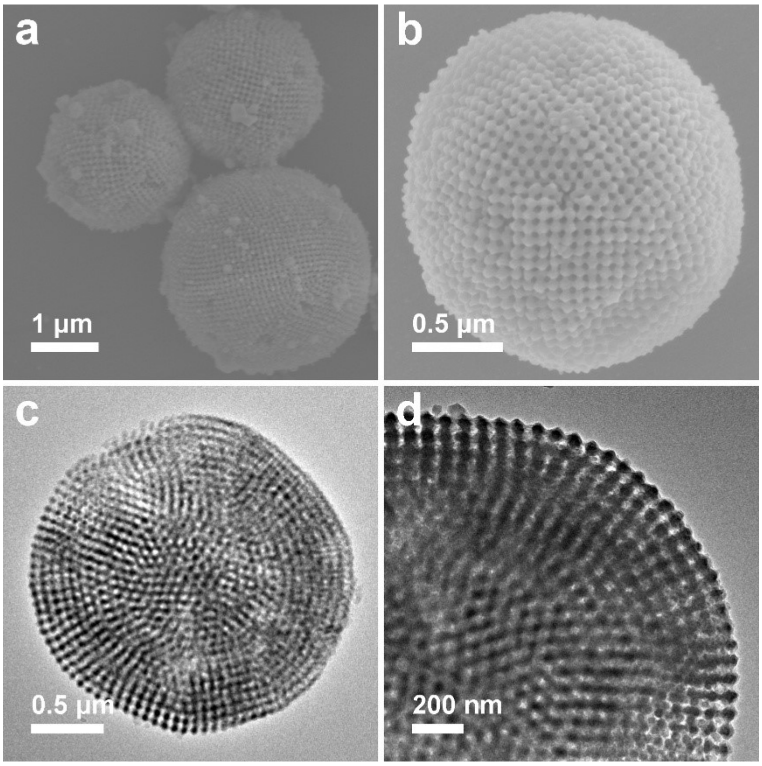

Fig. S8 (a,b) SEM and (c,d) TEM images of ZIF-8@ZIF-67 SPPs.

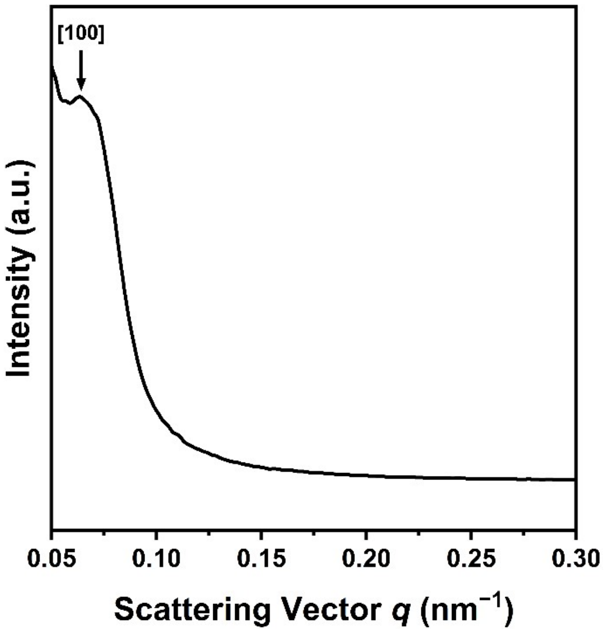

Fig. S9 SAXS pattern of ZIF-8@ZIF-67 SPPs.

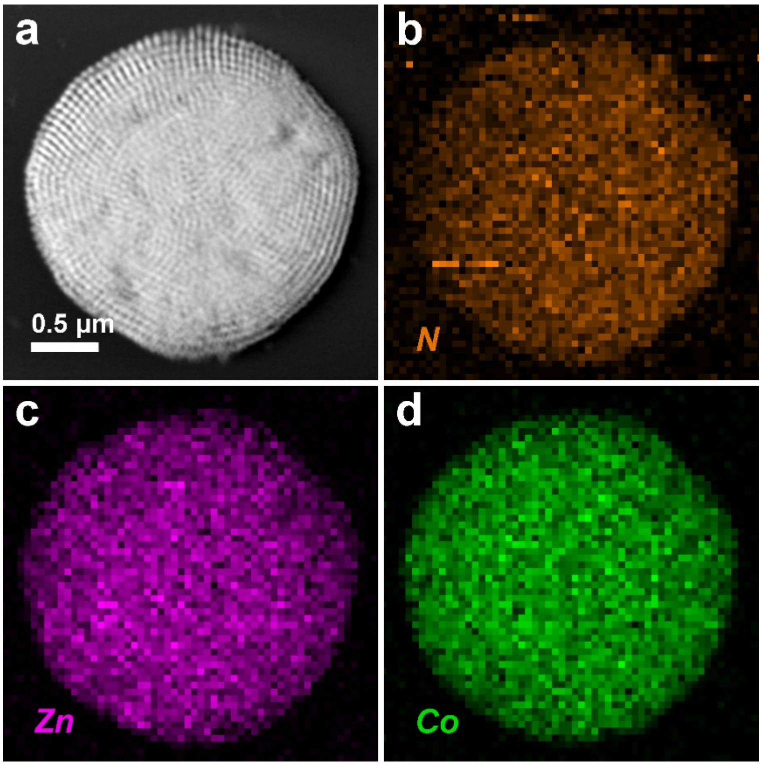

Fig. S10 HAADF-STEM and EDX elemental mapping images of a ZIF-8@ZIF-67 SPP.

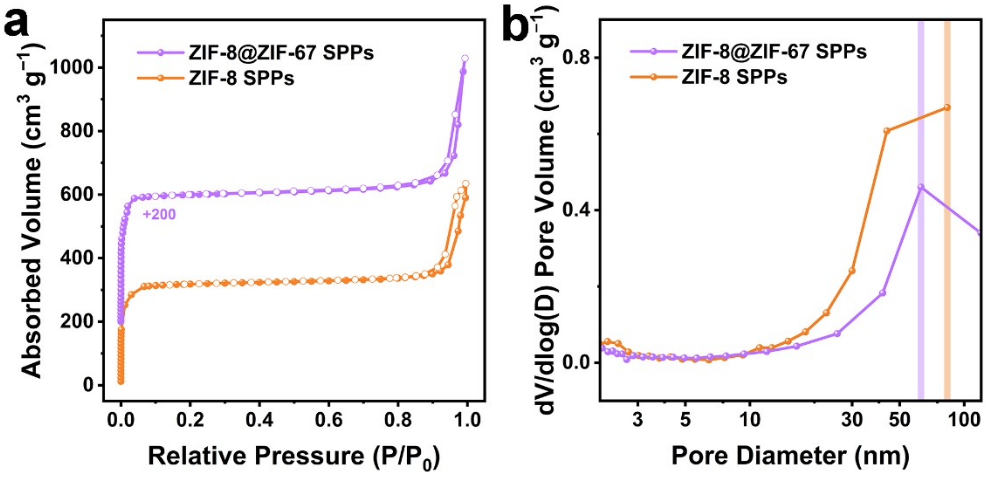

Fig. S11 (a) N_2 sorption isotherms and (b) pore size distribution analyses based on the BJH model of ZIF-8 SPPs and ZIF-8@ZIF-67 SPPs.

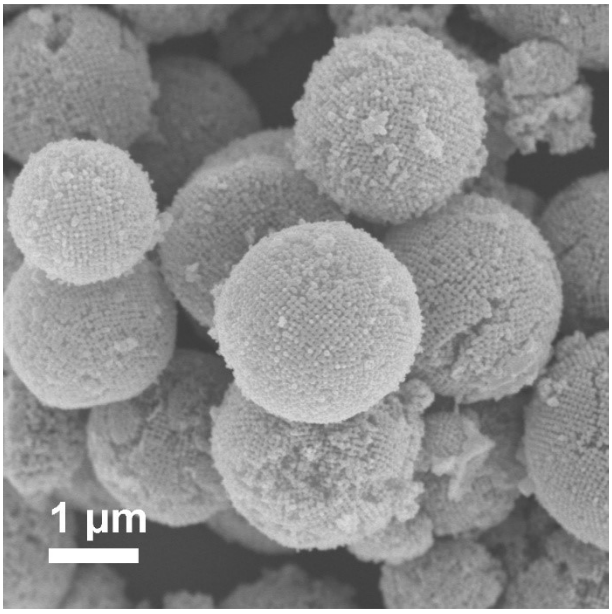

Fig. S12 Low-magnification SEM image of Co/NC UDPPs.

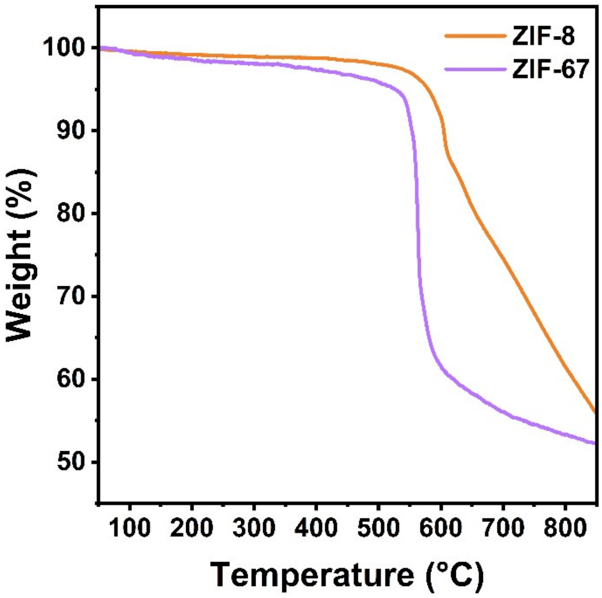

Fig. S13 Thermogravimetric curves of ZIF-8 and ZIF-67 in the flowing N_2 with a heating rate of 5 °C min^{-1}.

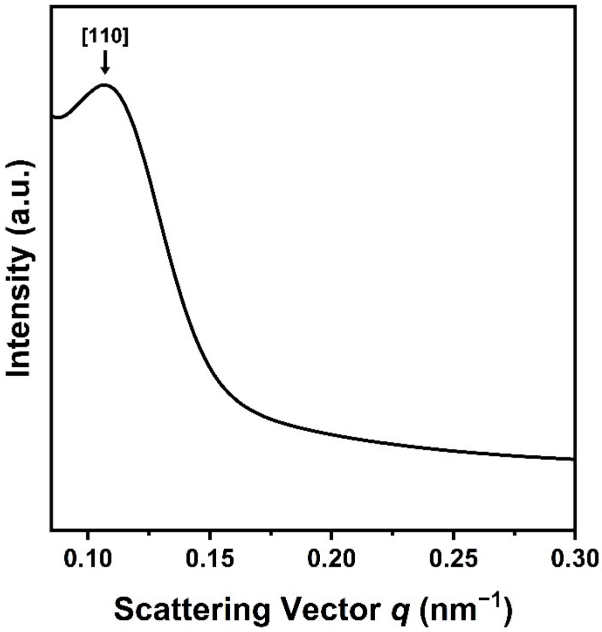

Fig. S14 SAXS pattern of Co/NC UDPPs.

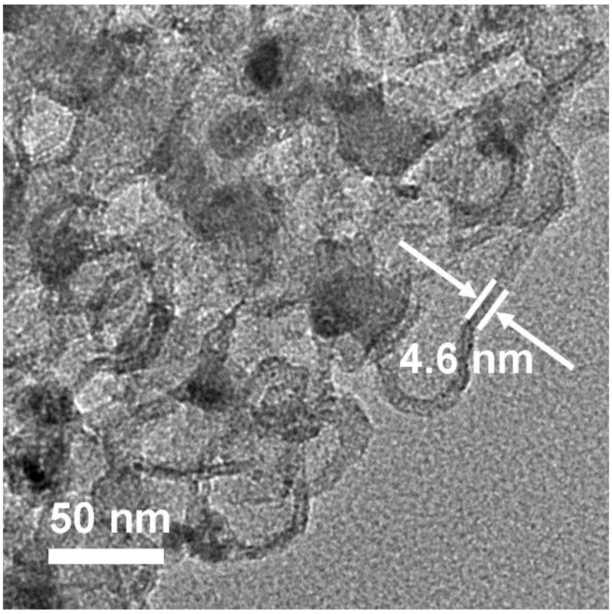

Fig. S15 TEM image of the edge of a Co/NC UDPP.

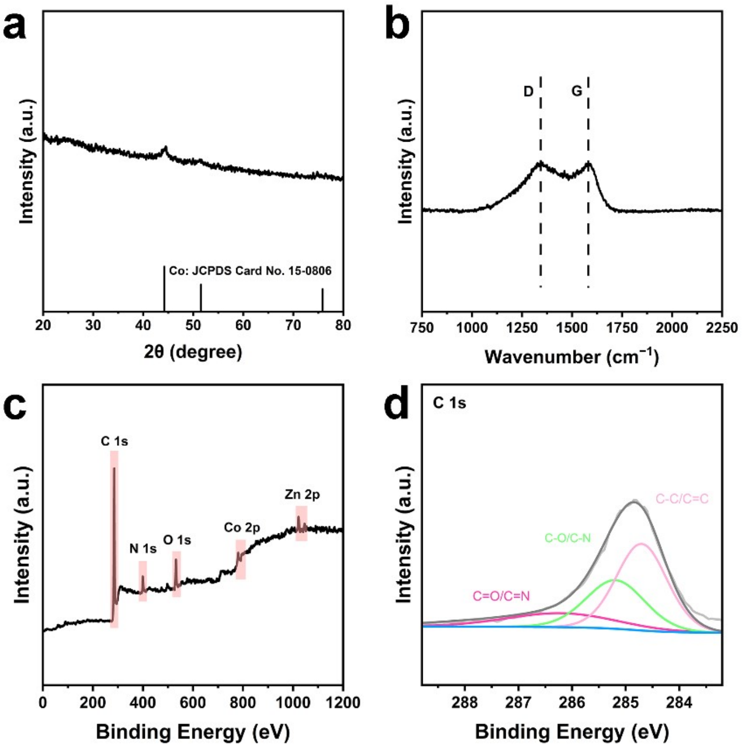

Fig. S16 (a) XRD pattern, (b) Raman spectrum, (c) XPS survey spectrum, and (d) high-resolution C 1s XPS spectrum of Co/NC UDPPs.

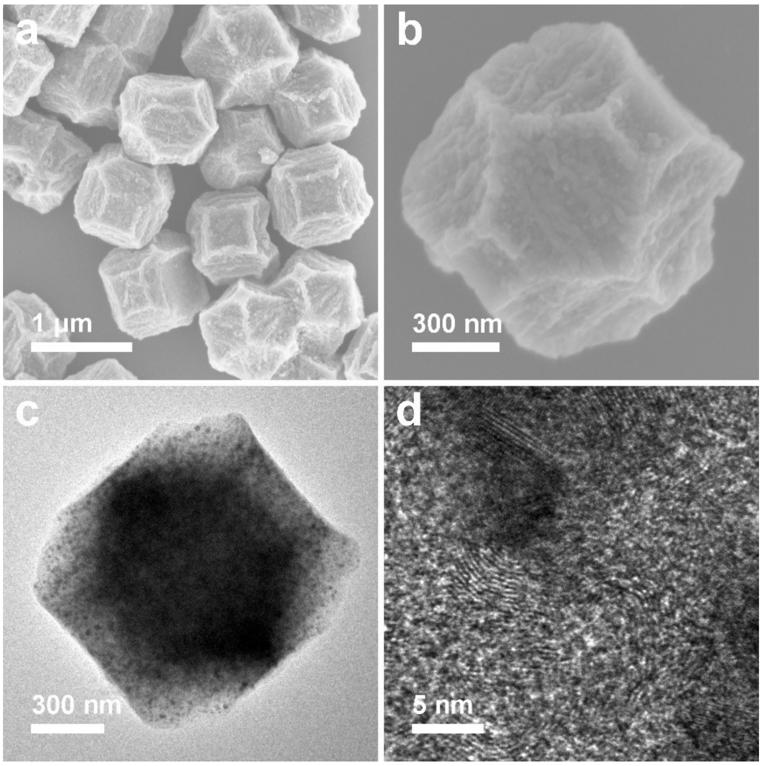

Fig. S17 (a,b) SEM, (c) TEM, and (d) HRTEM images of Co/NC SPs.

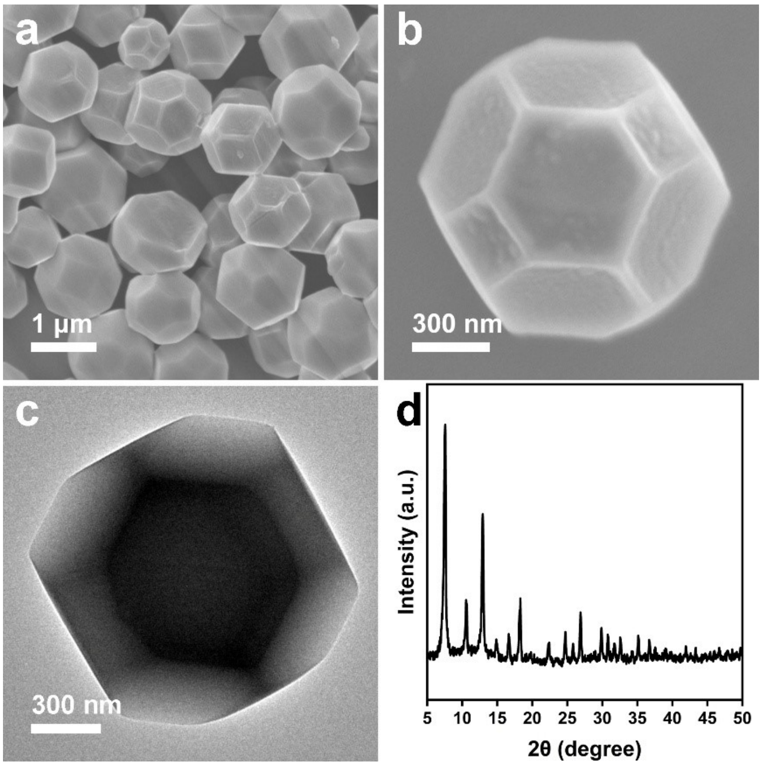

Fig. S18 (a,b) SEM images, (c) TEM image, and (d) XRD pattern of ZIF-67 crystals.

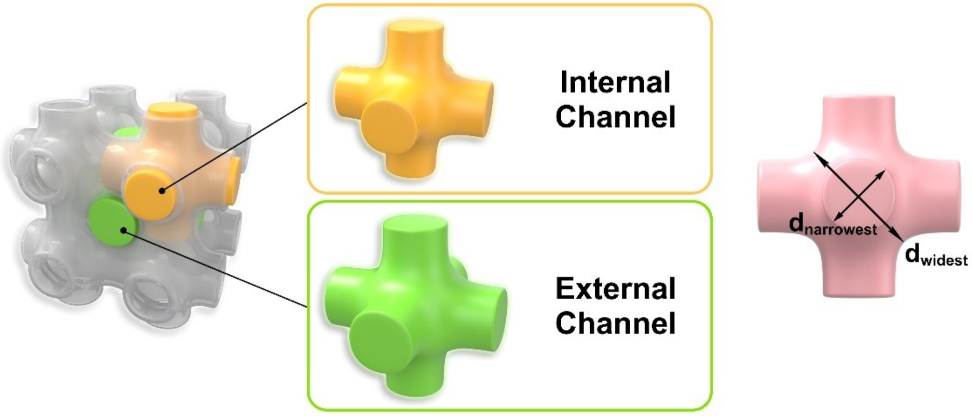

Fig. S19 The channel models of a Co/NC UDPP.

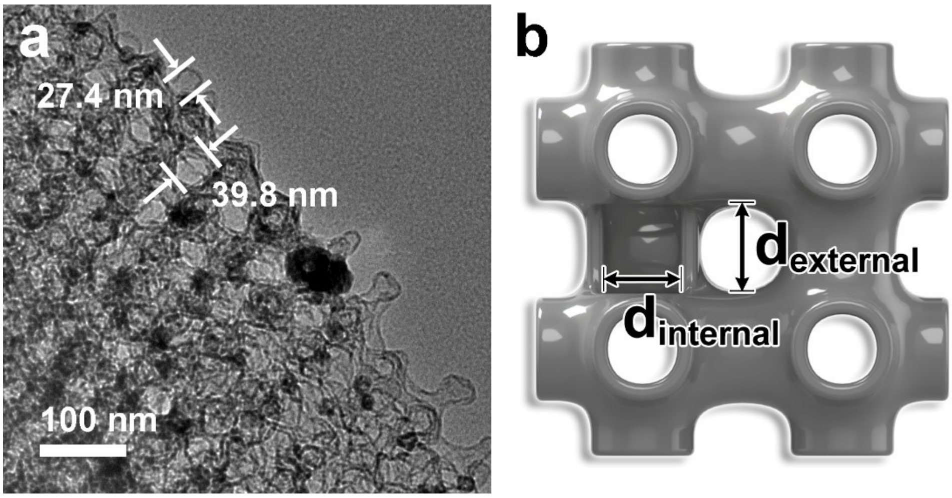

Fig. S20 (a) High-magnification TEM image and (b) corresponding model of a Co/NC UDPP for measuring the pore sizes of the internal and external channels at their narrowest positions.

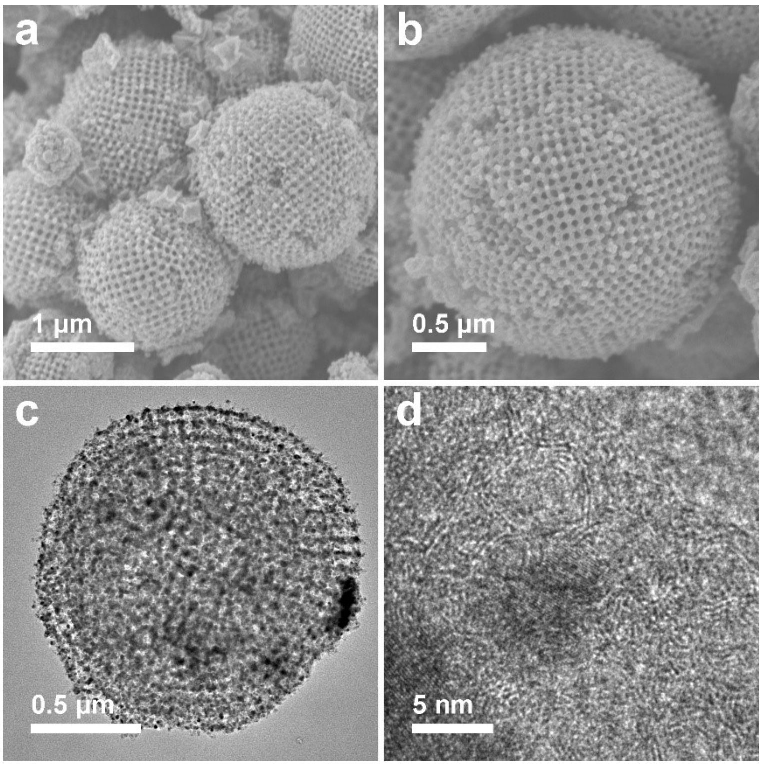

Fig. S21 (a,b) SEM, (c) TEM, and (d) HRTEM images of Co/NC SPPs.

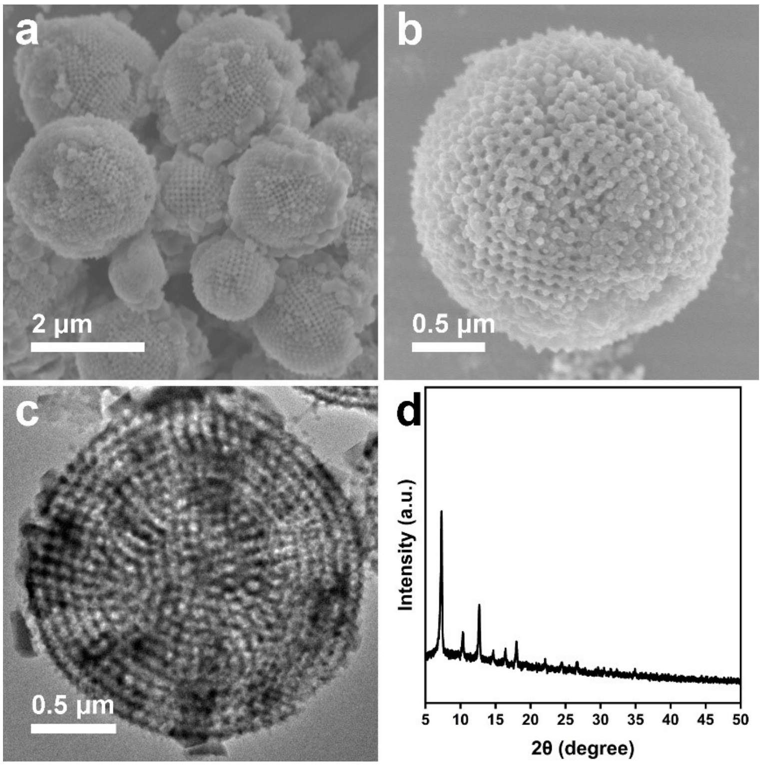

Fig. S22 (a,b) SEM images, (c) TEM image, and (d) XRD pattern of ZIF-67 SPPs.

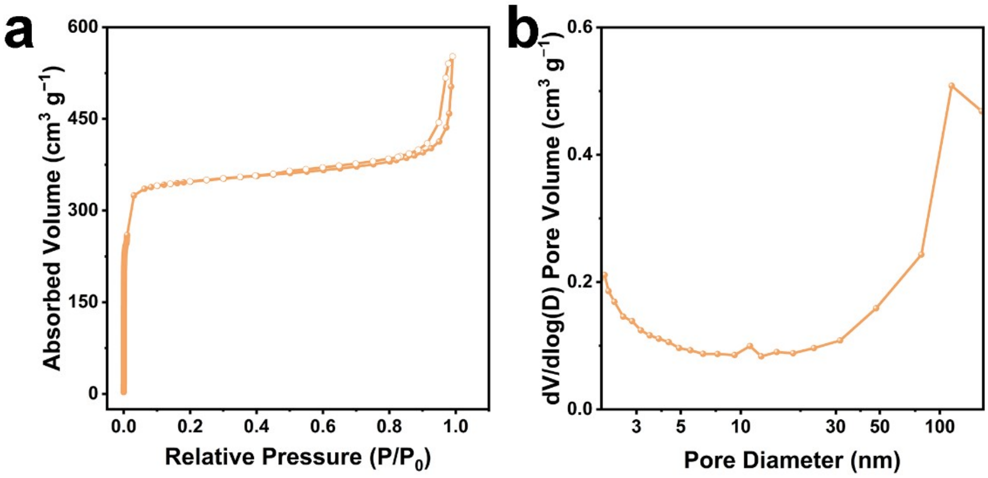

Fig. S23 (a) N_2 sorption isotherms and (b) pore size distribution analysis based on the BJH model of ZIF-67 SPPs.

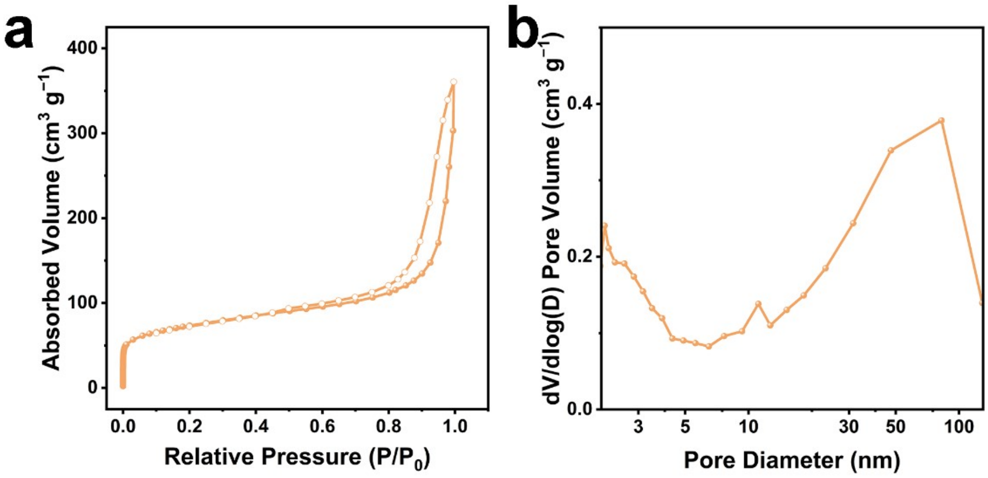

Fig. S24 (a) N_2 sorption isotherms and (b) pore size distribution analysis based on the BJH model of Co/NC SPPs.

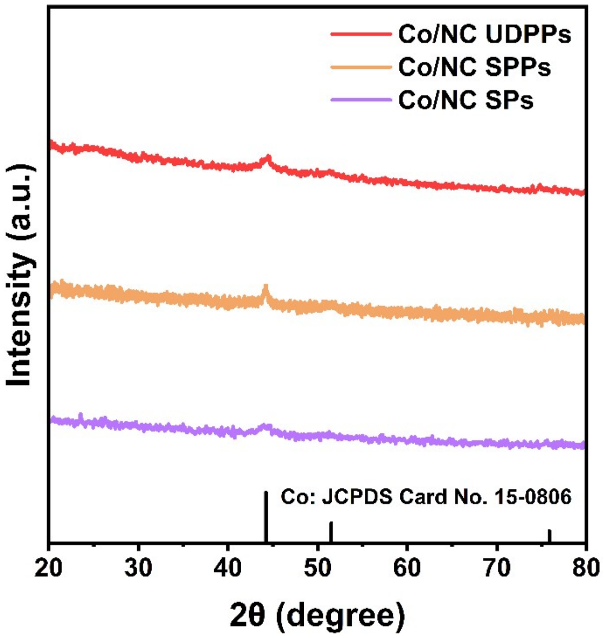

Fig. S25 XRD patterns of Co/NC SPs, Co/NC SPPs, and Co/NC UDPPs.

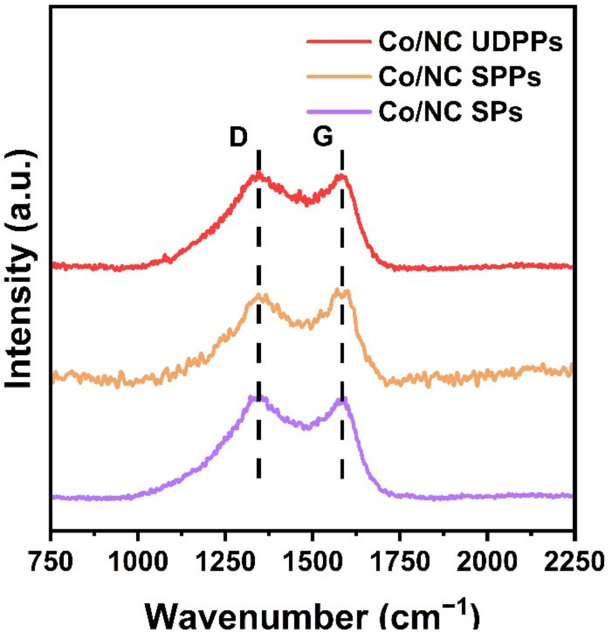

Fig. S26 Raman spectra of Co/NC SPs, Co/NC HPs, and Co/NC UDPPs.

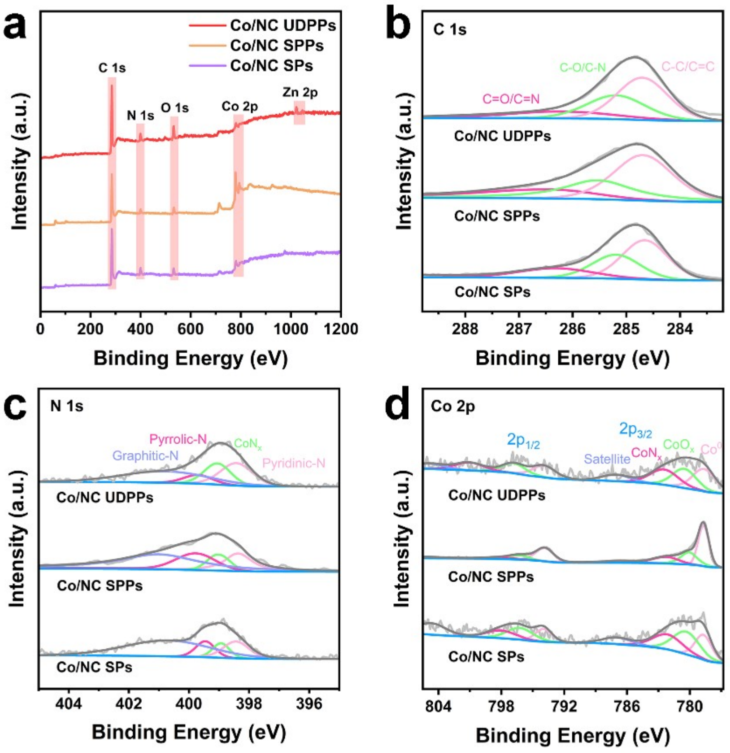

Fig. S27 (a) XPS survey spectra, high-resolution (b) C 1s, (c) N 1s, and (d) Co 2p spectra of Co/NC SPs, Co/NC SPPs, and Co/NC UDPPs.

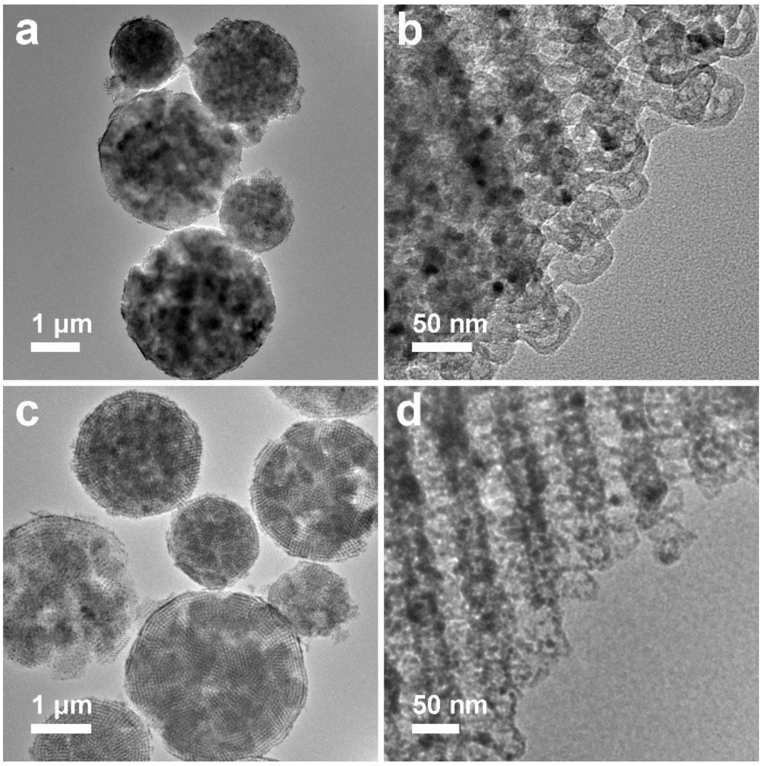

Fig. S28 TEM images of Co/NC UDPPs synthesized with different calcination temperatures: (a,b) 600 °C and (c,d) 800 °C.

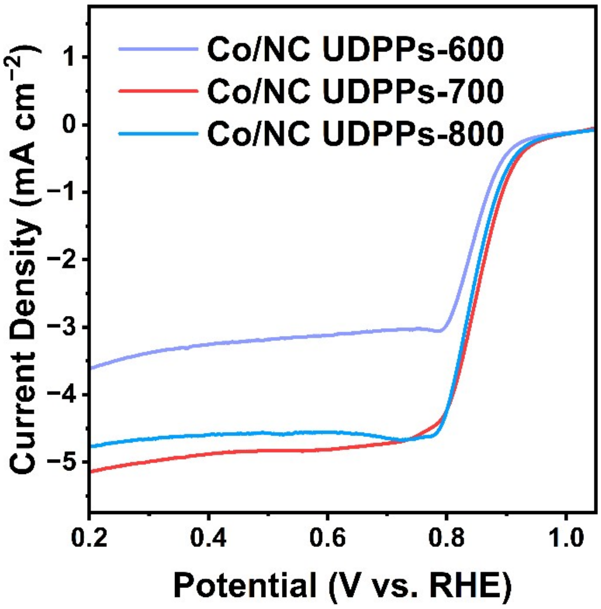

Fig. S29 LSV curves for Co/NC UDPPs-T (T represents the calcination temperature) in O_2-saturated 0.1 M KOH with a rotating rate of 1600 rpm.

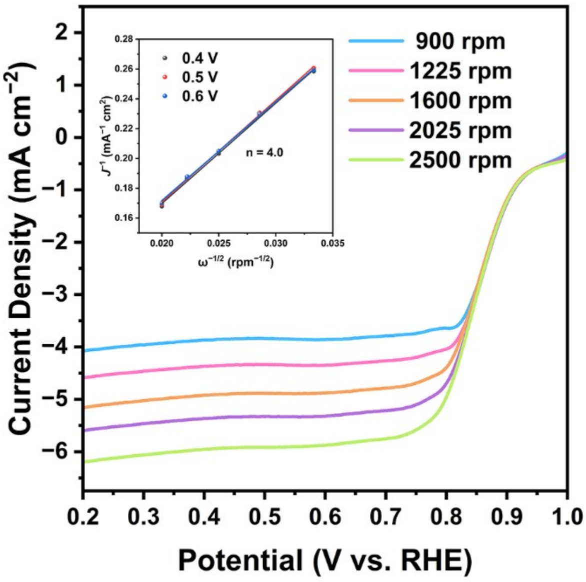

Fig. S30 The LSV curves at different rotating rates of Co/NC UDPPs (inset: derived K-L plot from the LSV curves at 0.4 V, 0.5 V, and 0.6 V vs. RHE).

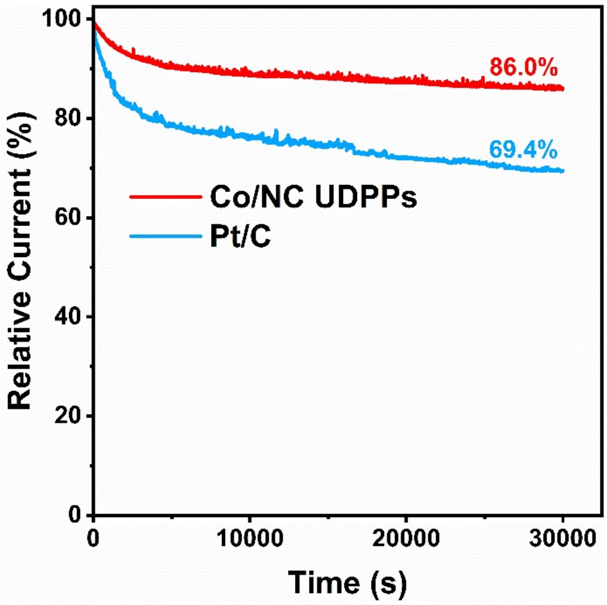

Fig. S31 Normalized chronoamperometry curves of Co/NC UDPPs and Pt/C tested for 30000 s.

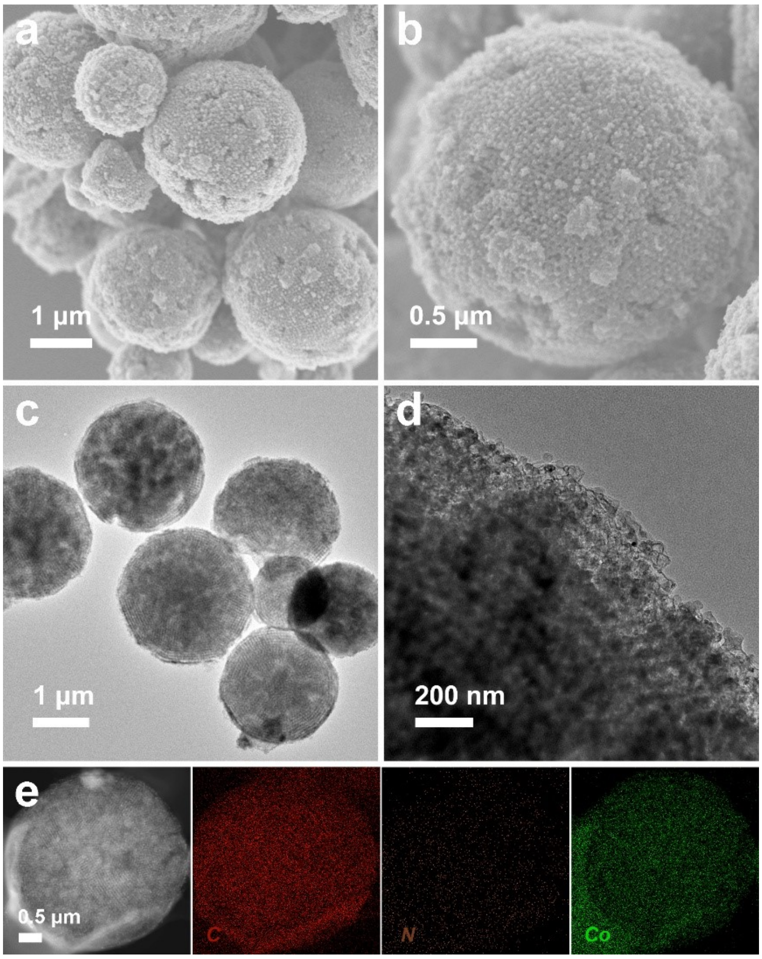

Fig. S32 (a,b) SEM, (c,d) TEM, (e) HAADF-STEM and EDX elemental mapping images of Co/NC UDPPs after the electrochemical reaction.

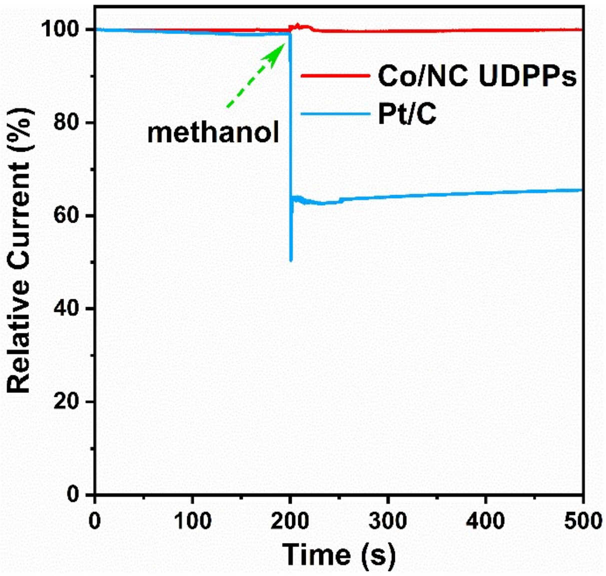

Fig. S33 Methanol tolerance test of Co/NC UDPPs and Pt/C with a rotating rate of 1600 rpm.

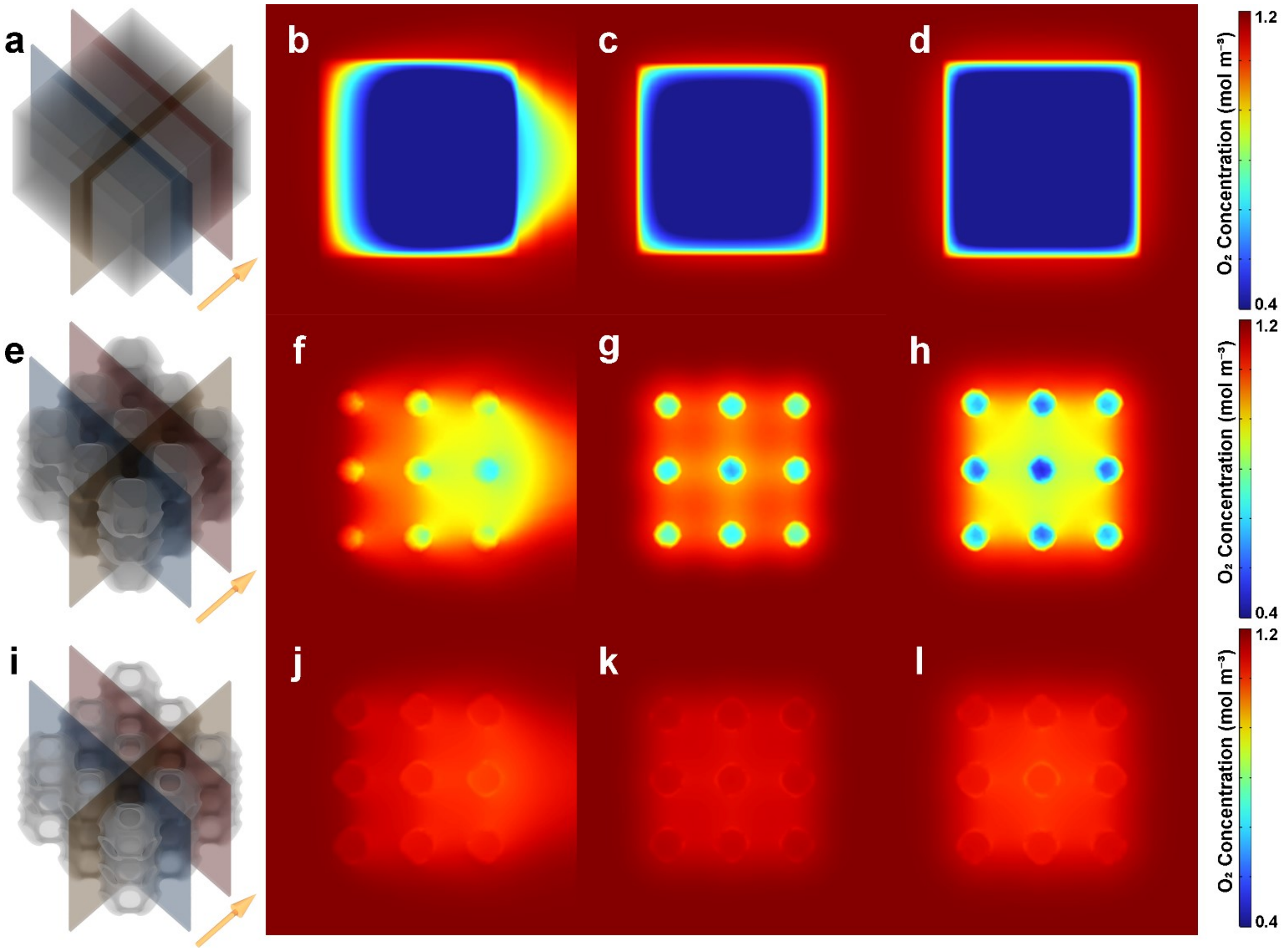

Fig. S34 (a,e,i) Schemes of simulation models and (b-d,f-h,j-l) sections illustrating O_2 concentrations in different directions for (a-d) Co/NC SP, (e-h) Co/NC SPP, and (i-l) Co/NC UDPP (yellow sections: b,f,j; blue sections: c,g,k; red sections: d,h,l).

Note: The arrows represent the direction of the liquid flow. As the depth of the sections increases along the liquid flow direction in corresponding models, the O_2 concentration decreases significantly.

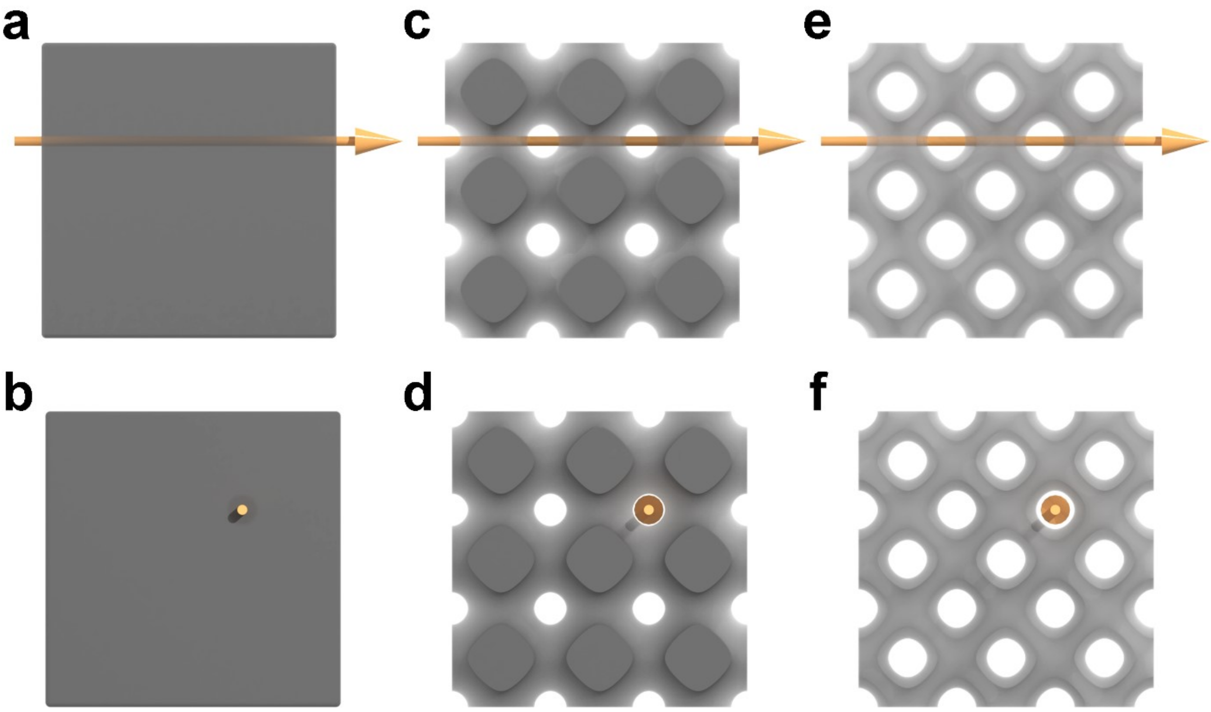

Fig. S35 Schemes of arrows along the direction of liquid flow for (a,b) Co/NC SP, (c,d) Co/NC SPP, and (e,f) Co/NC UDPP.

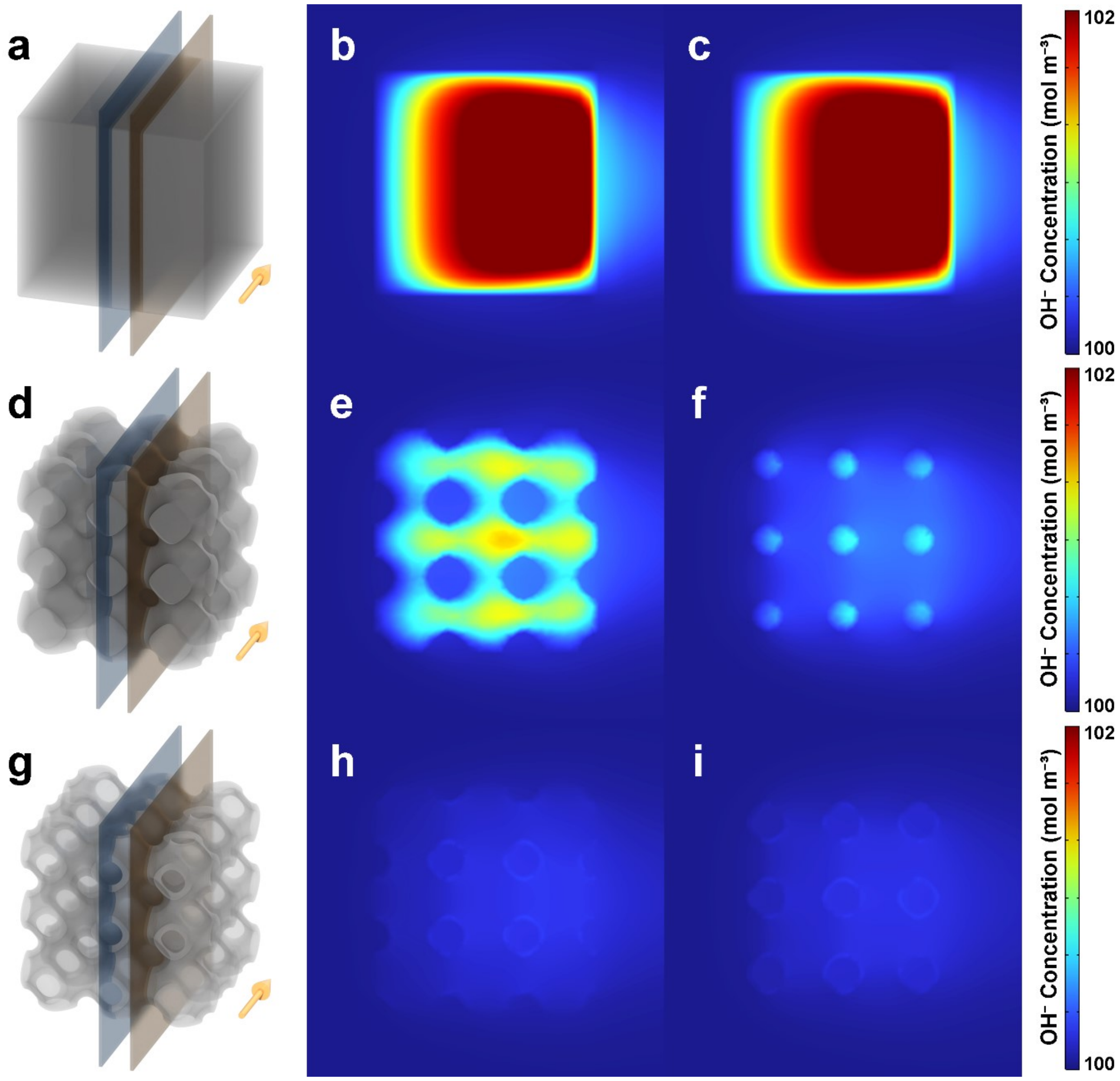

Fig. S36 (a,d,g) Schemes of simulation models and (b,c,e,f,h,i) sections illustrating OH^- concentrations in different directions for (a-c) Co/NC SP, (d-f) Co/NC SPP, and (g-i) Co/NC UDPP (blue sections: b,e,h; yellow sections: c,f,i).

Note: The arrows represent the direction of the liquid flow.

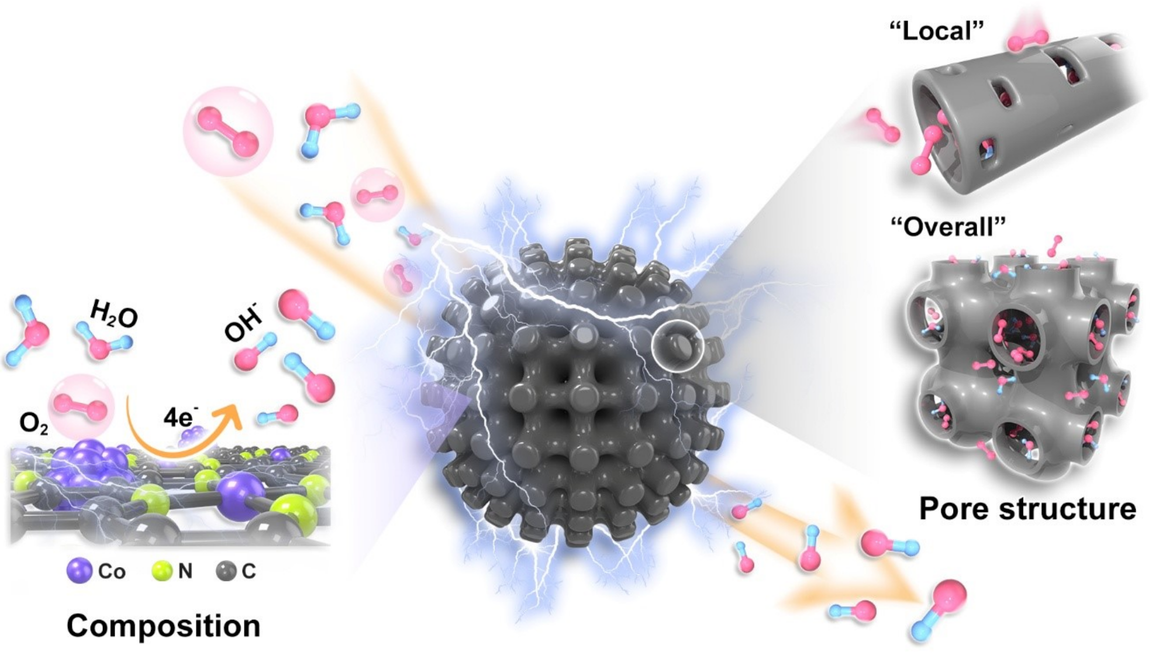

Fig. S37 Schematic illustration of the ORR catalyzed in a Co/NC UDPP.

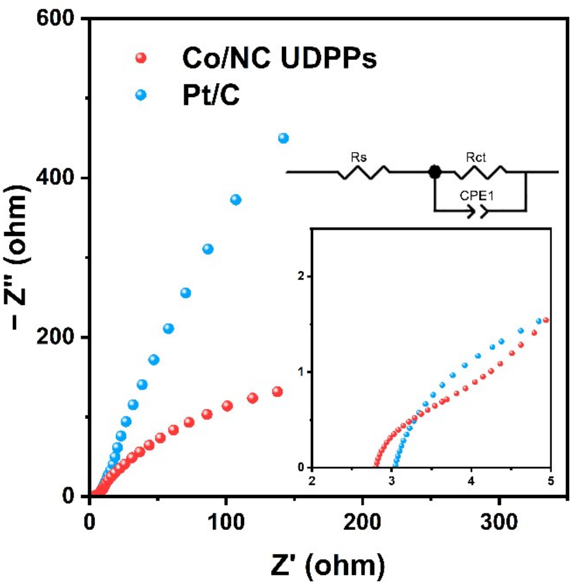

Fig. S38 Electrochemical impedance spectroscopy measurements of Co/NC UDPPs and Pt/C. The inset shows the equivalent circuit, where Rs represents ohmic resistance, Rct denotes charge transfer resistance, CPE1 is constant phase element.

Section 3. Supplementary Tables

Table S1. Textural properties of different samples.

Sample	S_{BET}[a] (m^2 g^{-1})	V_{total}[b] (cm^3 g^{-1})	V_{micro}[c] (cm^3 g^{-1})	V_{meso}[d] (cm^3 g^{-1})
ZIF-8 SPPs	1043	0.98	0.45	0.45
ZIF-8@ZIF-67 SPPs	1722	1.24	0.59	0.65
ZIF-67 SPPs	1164	0.85	0.47	0.38
Co/NC SPs	376	0.22	0.14	0.11
Co/NC SPPs	265	0.50	0.04	0.43
Co/NC UDPPs	355	0.67	0.08	0.57

[a] S_{BET} (total surface area) calculated by applying the BET equation using the linear part ($0.05 < P/P_0 < 0.30$) of the adsorption isotherm.

[b] V_{total} (total pore volume) calculated by single point adsorption total pore volume of pores at $P/P_0 = 0.99$.

[c] V_{micro} (micropore volume) calculated using the t-plot method.

[d] V_{meso} (mesopore volume) calculated using BJH method.

Table S2. Comparison of ORR catalytic activity between Co/NC UDPPs and cobalt-based materials in the literature.

Catalyst	$E_{1/2}$ (V)	Reference
Co/NC UDPPs	0.856	This work
H-3DOM-Co/ONC	0.841	2
FeCo-NPC	0.83	3
Nd/Co@NC	0.85	4
O-Co-N/C	0.85	5
OLC/Co-N-C	0.855	6
Co-SAs@NC	0.82	7
MnO@CNT@Co-N/C	0.81	8
C-Zn/Co_{800}	0.86	9

Table S3. Comparison of the performances of the Zn-air batteries with Co/NC UDPPs and cobalt-based materials as the air-cathode catalysts in the literature.

Catalyst	Peak power density (mW cm^{-2})	References
Co/NC UDPPs	215	This work
FeCo-NPC	165	3
Nd/Co@NC	70.6	4
O-Co-N/C	143	5
Co-SAs@NC	105.3	7
Co@DMOF-900	158	10
Co SA/NCFs	154.5	11
MS-Co$_{SA}$-N-C-800°C	160	12
Zn/CoN-C	230	13

Table S4. R_s and R_{ct} of Co/NC UDPPs and Pt/C.

Sample	R_s (ohm)	R_{ct} (ohm)
Co/NC UDPPs	2.75	1.78
Pt/C	2.97	3.65

Supplementary references

1. Y. Deng, T. Yu, Y. Wan, Y. Shi, Y. Meng, D. Gu, L. Zhang, Y. Huang, C. Liu, X. Wu and D. Zhao, *J. Am. Chem. Soc.*, 2007, **129**, 1690-1697.
2. W. Yao, A. Hu, J. Ding, N. Wang, Z. Qin, X. Yang, K. Shen, L. Chen and Y. Li, *Adv. Mater.*, 2023, **35**, 2301894.
3. Z. Pei, H. Zhang, Y. Guo, D. Luan, X. Gu and X. W. Lou, *Adv. Mater.*, 2024, **36**, 2306047.
4. C. Fan, X. Wang, X. Wu, Y. Chen, Z. Wang, M. Li, D. Sun, Y. Tang and G. Fu, *Adv. Energy Mater.*, 2023, **13**, 2203244.
5. W. Zhang, C.-H. Xu, H. Zheng, R. Li and K. Zhou, *Adv. Funct. Mater.*, 2022, **32**, 2200763.
6. Z. Liang, N. Kong, C. Yang, W. Zhang, H. Zheng, H. Lin and R. Cao, *Angew. Chem., Int. Ed.*, 2021, **60**, 12759-12764.
7. X. Han, X. Ling, Y. Wang, T. Ma, C. Zhong, W. Hu and Y. Deng, *Angew. Chem., Int. Ed.*, 2019, **58**, 5359-5364.
8. F. Li, T. Qin, Y. Sun, R. Jiang, J. Yuan, X. Liu and A. P. O'Mullane, *J. Mater. Chem. A*, 2021, **9**, 22533-22543.
9. X. Yang, X. Li, M. Liu, S. Yang, Q. Xu and G. Zeng, *Small*, 2024, **20**, 2306295.
10. S. Yuan, J. Zhang, L. Hu, J. Li, S. Li, Y. Gao, Q. Zhang, L. Gu, W. Yang, X. Feng and B. Wang, *Angew. Chem., Int. Ed.*, 2021, **60**, 21685-21690.
11. Y. Han, H. Duan, C. Zhou, H. Meng, Q. Jiang, B. Wang, W. Yan and R. Zhang, *Nano Lett.*, 2022, **22**, 2497-2505.
12. K. Wang, Z. Lu, J. Lei, Z. Liu, Y. Li and Y. Cao, *ACS Nano*, 2022, **16**, 11944-11956.
13. Z. Lu, B. Wang, Y. Hu, W. Liu, Y. Zhao, R. Yang, Z. Li, J. Luo, B. Chi, Z. Jiang, M. Li, S. Mu, S. Liao, J. Zhang and X. Sun, *Angew. Chem., Int. Ed.*, 2019, **58**, 2622-2626.